RESEARCH

A closed-form correction for three-point bend testing of functionally graded beams, with application to endovascular devices

Charles B. Suskin[1−5†], Juan J. Becerra-Garcia[1−4†], Yosef E. Granillo[1−4†], Michael Y. Qiu[1−5], Yuxuan Huang[3−4], Mohamed A. Zayed[1−3,5*], Joshua W. Osbun[1−2*] and Guy M. Genin[1−4*]

[1]*Center for CardioVascular Research Innovation in Surgery & Engineering, Washington Univ., St. Louis, MO 63130, USA*
[2]*Div. of Neurotechnology, Dept. of Neurological Surgery, Washington Univ., St. Louis, MO 63110, USA*
[3]*Dept. of Biomedical Engineering, Washington Univ. in St. Louis, St. Louis, MO 63130, USA*
[4]*NSF Science and Technology Center for Engineering Mechanobiology, Dept. of Mechanical Engineering & Materials Science, Washington Univ., St. Louis, MO 63130, USA*
[5]*Section of Vascular Surgery, Department of Surgery, Washington Univ., St. Louis, MO 63110, USA*
† *These authors contributed equally to this work.*

Abstract. Three-point bend testing offers simple, non-destructive quantification of the flexural rigidity of a slender structure, but the single apparent stiffness that it returns misrepresents the true local properties if flexural rigidity varies along the span. The error can be severe in structures with deliberately engineered stiffness gradients, such as endovascular catheters and guidewires whose graded transition zones govern clinical performance, and which are thus the regions most in need of accurate characterization. We solve the Euler-Bernoulli bending of a linearly graded beam in closed form and show that the true midspan rigidity exceeds the apparent value by a correction factor with the compact expansion

$W = 1 + m^2/10 + O(m^4)$, where m is the dimensionless change in stiffness across the support span. The leading measurement error term therefore grows quadratically with the local gradient. To recover m from discrete, noisy data we estimate the local gradient by windowed linear regression with optional Gaussian pre-smoothing, and identify the sampling and smoothing needed for stable inversion. On synthetic profiles spanning the gradient range of real devices, the correction reduces transition-zone error from as much as 10% to a fraction of a percent; applied to a commercial graded long sheath it removes a systematic transition-zone bias of order 1%. We further distinguish where the correction helps and where standard three-point testing already suffices, yielding a simple decision rule for the recovery of local properties from bending of any functionally graded beam.

Subject Areas: Biomechanics, Medical devices, Mechanical testing

Keywords: flexural rigidity, endovascular devices, three-point bending, functionally graded materials, catheter mechanics

Author for correspondence: Mohamed A. Zayed, Joshua W. Osbun, Guy M. Genin
genin@wustl.edu

1 Introduction

Endovascular procedures have transformed the treatment of vascular disease, replacing open surgery with treatment delivered to distal targets via minimally invasive navigation of a coaxial system of guidewires, catheters, intermediate guide catheters, and long sheaths [1–3]. The success of this navigation hinges on the flexural rigidity of these devices: too much stored elastic energy and the device herniates out of the intended path at a sharp bend (Fig. 1a) [4]; too much or too little flexural rigidity and it cannot track through tortuous anatomy [5]. Manufacturers therefore engineer the flexural rigidity to vary along the length, typically with a compliant distal tip for navigation that grades into a stiffer proximal body for support and pushability [6]. The resulting transition zone design (Fig. 1b) frequently determines whether a procedure succeeds [7]. These engineered gradients arise from manufactured features across the intricate, multilayered construction of endovascular devices. They must be characterized along their length by non-destructive testing. Manufacturers rarely publish quantitative flexural rigidity data, leaving interventionalists to rely on experience and qualitative feel when selecting devices [8, 9]. Cantilever methods give a direct flexural rigidity but require destructive sectioning and cannot readily resolve a continuous transition zone [6, 10]. The three-point bend test (Fig. 1c) is the natural alternative: non-destructive, simple, and able to profile flexural rigidity point by point along the full length [11, 12]. The standard three-point bend formula, however, assumes uniform flexural rigidity. Applied to a beam whose flexural rigidity varies appreciably over the support span, it returns a biased apparent flexural rigidity that blurs the transition zones that are of greatest interest. The underlying forward problem, namely the bending of beams with spatially varying flexural rigidity, is classical and has been solved many times. Closed-form and series solutions for non-prismatic and variable-rigidity beams date back decades [13–15] and continue to be refined [16, 17]. The problem is central to the mechanics of functionally graded materials, beginning with Sankar's elasticity solution for graded beams [18]; a substantial literature has since developed closed-form and semi-analytical treatments of beams whose stiffness varies along the axis, so-called axially functionally graded or tapered beams [19, 20]. Elishakoff and co-workers, in particular, obtained closed-form solutions for inhomogeneous beams by treating the stiffness distribution itself as the unknown [21, 22]; this semi-inverse construction is conceptually related to the closed-form correction developed here, although distinct in purpose. The same forward problem recurs throughout engineering and nature: in wedges and cones [23], in graded engineered structures from bridge girders to fracture specimens [24, 25], and in graded biological beams such as plant stalks and bone [16, 26–30]. Our aim is orthogonal to this body of work: we do not re-solve the forward problem, but invert it. In nearly every setting above, the gradient is either known *a priori* or is the incidental consequence of geometry, and the quantity sought is the structure's response. The endovascular setting is distinctive in that the gradient is deliberately introduced during manufacture and must then be recovered from a routine measurement to use the device effectively. This is an inverse problem: given a profile of apparent rigidities measured by three-point bending, recover the true local flexural rigidity and its gradient. Identification of a spatially varying flexural rigidity from deflection data is known to be ill-posed and is conventionally approached numerically [31]. We instead exploit the specific structure of the catheter problem, with small, slowly varying gradients, to obtain a closed-form correction with an explicit error estimate that can be applied retroactively to existing measurements. We derive, from Euler-Bernoulli theory, a closed-form correction relating the apparent midspan flexural rigidity to the true value for a linearly graded beam, together with a compact error estimate that guides test design. We show that the correction reduces to the simple form $1 + m^2/10$ over the gradient range relevant to commercial devices, where m, defined in the next section, represents the steepness of the gradient over the test length. We develop a robust scheme for estimating the local gradient from discrete and noisy measurements, and validate the method against analytical benchmarks and demonstrate it on a commercial endovascular device. The correction requires no new equipment and applies retroactively to existing three-point bend data.

2 Methods

2.1 Experimental setup for three-point bend testing

Flexural rigidity was measured along the length of each device using an automated three-point bend apparatus described by Qiu et al. [11]. The apparatus differs from a conventional universal testing machine in that it indexes the specimen longitudinally between measurements, allowing the flexural rigidity to be profiled point by point along an endovascular device and thereby resolving the transition zones that are the focus of this study (Fig. 1c). The apparatus was built from a three-axis CNC router (Genmitsu 3018-PROVer, SainSmart, Las Vegas, NV). A load cell (SparkFun TAL221, 0.5 kg capacity, SparkFun Electronics, Niwot, CO) was mounted to the Z-axis carriage and connected through a 24-bit amplifier (SparkFun HX711) to a microcontroller (Arduino Uno Rev3) that recorded force throughout each loading cycle. The system resolved forces to approximately 0.02 mN at a sampling rate of 10 Hz, and resolved carriage displacement to 1.25 μm per step. Bending was applied in a symmetric three-point configuration. The specimen rested on two fixed cylindrical supports (6 mm diameter) separated by a span L, set to 30 mm. A third cylinder, mounted on the load cell at the Z-axis carriage, served as the loading nose and descended onto the specimen at midspan. Because endovascular devices are slender and laterally compliant, a pair of guide rollers was positioned just above and offset from the supports to keep the specimen seated during loading without contributing to the measured force. Longitudinal profiling was achieved by advancing the specimen to successive measurement stations between loading cycles. At each station the loading nose descended at 0.5 mm/s to a fixed midspan deflection of 2 mm, was held for 5 s while the steady-state force was recorded, and then retracted before the specimen was indexed to the next station. This automation enabled dense, repeatable sampling through transition zones where flexural rigidity changes most rapidly (see Section 2.2).

2.2 Testing protocol

As a demonstration on a commercial device with a clinically relevant stiffness gradient, we profiled a single 088 Neuron MAX long sheath (Penumbra, Inc., Alameda, CA) along its entire length. The full-length profile was acquired three times, with the device repositioned between repeats to assess measurement repeatability. Measurement stations were spaced adaptively along the device. Because the accuracy of the estimated gradient, and therefore of the correction factor, depends on the station spacing relative to the length scale over which the flexural rigidity varies (Section 3.2), we sampled at $\sim$5 cm intervals over nominally uniform segments and refined to $\sim$1 cm intervals through transition zones, identified as regions in which the apparent flexural rigidity changed rapidly between successive stations. At each station the device was loaded through the cycle described in Section 2.1, and the force-deflection response was recorded continuously. All testing was confined to the linear, recoverable regime assumed by the analysis. The force-deflection response was confirmed to be linear over the working range, and full elastic recovery of the specimen was verified after each cycle; the quantitative criteria used to extract flexural rigidity from these records are given in Section 2.4.

2.3 Analytical correction for linearly graded beams

2.3.1 Bending of a linearly graded beam

In a conventional three-point bend test the specimen is treated as uniform, and its flexural rigidity is inferred from the measured central deflection δ under a central load F on a span L using the Euler-Bernoulli result [32],

$$B_0 = \frac{FL^3}{48\,\delta}. \tag{1}$$

We call B_0 the apparent flexural rigidity, because for a non-uniform specimen it is a weighted average over the span rather than a local property. To model a transition zone we take the flexural rigidity to vary linearly

across the span:

$$B(x) = B_m\left(1 + \frac{2mx}{L}\right), \tag{2}$$

where x is measured from the loading point at midspan, $B_m = B(0)$ is the true flexural rigidity at midspan, and the supports lie at $x = \pm L/2$. The dimensionless gradient m is fixed by Eq. (2): the flexural rigidity takes the values $B_m(1 \pm m)$ at the two supports, so that $m = (L/2)B'(x)/B_m$ is the slope of the flexural rigidity scaled by the half-span and the midspan flexural rigidity, in which $B'(x) = dB(x)/dx$. The bending moment is set by $M(x) = \frac{F}{2}\left(\frac{L}{2} - |x|\right)$, so the deflection obeys

$$B(x)\,\frac{\mathrm{d}^2 w}{\mathrm{d}x^2} = -\frac{F}{2}\left(\frac{L}{2} - |x|\right), \qquad -\frac{L}{2} \le x \le \frac{L}{2}, \tag{3}$$

where w is the deflection in the direction of the applied load. Introducing the normalized flexural rigidity coordinate $Y = 1 + 2mx/L$ (so that $B = B_m Y$) and the reference deflection $w_0 = FL^3/(48B_m)$ of a uniform beam of flexural rigidity B_m, Eq. (3) integrates in closed form (Appendix A). Imposing zero deflection at the supports and continuity of deflection and slope across the loading point gives the normalized central deflection $W(m) \equiv w(0)/w_0$,

$$W(m) = \frac{3}{2m^3}\Big[(1+m)^2\ln(1+m) - (1-m)^2\ln(1-m) - 2m\Big]. \tag{4}$$

2.3.2 Correction factor, small-gradient limit and measurement error

Since $W(m) = w(0)/w_0 = B_m/B_0$, the normalized deflection converts the apparent flexural rigidity into the true midspan flexural rigidity,

$$B_m = B_0\,W(m). \tag{5}$$

$W(m)$ is even in m and satisfies $W(m) \ge 1$; the apparent flexural rigidity therefore always underestimates the true midspan flexural rigidity, by an amount that depends only on the magnitude of the local gradient and not on its sign. Expanding Eq. (4) for small m,

$$W(m) = 1 + \frac{m^2}{10} + \frac{m^4}{35} + \frac{m^6}{84} + \frac{m^8}{165} + \cdots = \sum_{k=0}^{\infty} \frac{m^{2k}}{\binom{2k+3}{3}}, \tag{6}$$

so that to leading order $W(m) \approx 1 + m^2/10$.The fractional error incurred by ignoring the gradient follows from Eq. (5),

$$\frac{B_0 - B_m}{B_m} = \frac{1}{W(m)} - 1 \;\approx\; -\frac{m^2}{10}, \tag{7}$$

so the apparent flexural rigidity is low by approximately $100\,(m^2/10)\%$. The quadratic dependence makes error negligible for gentle gradients, but significant at sharp transitions.

2.3.3 Estimating the local gradient from a measured profile

Applying the correction requires the local gradient m at each station, which must itself be recovered from the measured profile of apparent rigidities. Adjacent-point finite differences are too sensitive to measurement noise to use directly; instead we estimate m from the local slope of the apparent-flexural rigidity profile obtained by linear regression over a symmetric window of stations,

$$m_i \approx \frac{L}{2B_i^0}\left(\frac{\mathrm{d}B^0}{\mathrm{d}x}\right)_w, \tag{8}$$

where B_i^0 is the apparent flexural rigidity at station i and $(\mathrm{d}B^0/\mathrm{d}x)_w$ is the regression slope over a window of n stations on either side. The window width trades resolution against noise rejection. It is widened where the profile is noisy or slowly varying and narrowed through sharp transitions, with asymmetric truncation near the ends. The window and the optional smoothing of noisy data are detailed in Section 2.4.

2.4 Data processing, gradient estimation and validation

At each measurement station the recorded force-deflection curve was reduced to a single apparent flexural rigidity. Forces were baseline-corrected against the pre-contact reading, the response over the 0.5–1.5 mm portion of the ramp was verified as being within the linear-elastic working range, and the stiffness $k = \mathrm{d}F/\mathrm{d}\delta$ was obtained by linear regression over this range. Only fits with coefficient of determination $R^2 > 0.98$ were retained. The apparent flexural rigidity then followed from the fitted stiffness as $B_0 = kL^3/48$, equivalent to Eq. (1) with F/δ replaced by the regression slope. The local gradient m at each station was estimated from the resulting profile of apparent rigidities using the windowed regression of Eq. (8). The half-width n of the regression window sets a trade-off: a narrow window follows sharp transitions faithfully but is sensitive to scatter, whereas a wide window suppresses scatter at the cost of blurring rapid changes in the gradient. We therefore matched the window to the profile, using the narrowest window consistent with the local noise level and widening it through regions where the gradient varies slowly. For profiles dominated by measurement noise, the apparent-flexural rigidity profile was first smoothed with a one-dimensional Gaussian filter (physical scale σ_s) before the slope was taken; without this step, high-frequency scatter propagates through Eq. (8) into m and is amplified rather than corrected by $W(m)$. Because the gradient in Eq. (8) must itself be estimated from the measured profile, the correction was applied iteratively, refining the gradient estimate while always correcting the original apparent reading. In the first pass the gradient $m^{(1)}$ was obtained from the apparent profile by the windowed regression of Eq. (8) (regression half-width $n = 2$ stations), and a first corrected profile was formed as $\hat{B}^{(1)}(x) = B_0(x)\,W\big(m^{(1)}\big)$. In each subsequent pass the gradient was re-estimated from the previous corrected profile, $m^{(j)} = (L/2)\,(\mathrm{d}\hat{B}^{(j-1)}/\mathrm{d}x)\big/\hat{B}^{(j-1)}$, and the correction was re-applied to the *same* apparent reading, $\hat{B}^{(j)}(x) = B_0(x)\,W\big(m^{(j)}\big)$. Because $W(m)$ always multiplies the fixed measured value rather than compounding onto the running estimate, the iteration refines only the gradient entering $W(m)$ and converges to a fixed point. A fixed number of passes was used rather than a convergence tolerance; results are reported after one, three and five iterations to display convergence. Although the correction is derived for a strictly linear gradient, the transition zones of real devices are smooth but non-linear. We therefore assessed the correction on three classes of synthetic profile: a linear gradient, for which the correction is exact and which serves as a benchmark; a logistic transition, representing the gradual stiffness change of a realistic transition zone; and a linear gradient with additive Gaussian noise (1, 3 and 5% of the mean flexural rigidity) to test robustness to measurement error. In each case a known true profile $B(x)$ was prescribed, the apparent profile $B_0(x)$ that a three-point bend test would report was computed at each measurement point by solving Eq. (3). The correction was applied, and the recovered flexural rigidity was then compared with the prescribed truth. A narrow window was used for the linear benchmark and progressively wider windows, with Gaussian pre-smoothing in the noisy case, for the logistic and noisy profiles. Error metrics are defined in Section 2.5.

2.5 Error metrics and repeatability

Because a single long sheath was characterized, the experimental analysis quantifies measurement precision rather than inter-device variation. Accuracy against a known ground truth was assessed only on the synthetic profiles, where the true flexural rigidity is prescribed. For the physical device, repeatability was assessed by profiling the device three times with repositioning between repeats. The precision at each measurement point was summarized by the coefficient of variation (the standard deviation divided by the mean of the apparent flexural rigidity across repeats) and repeated-measurement values are reported as mean $\pm$ standard deviation. No ground-truth flexural rigidity exists for the real device, so we report only precision and the magnitude of the correction, not accuracy. For the synthetic profiles (Section 2.4), the true profile $B(x)$ is known, and the accuracy of the correction was quantified by the mean absolute percentage error between the recovered and

true rigidities over the N stations,

$$\mathrm{MAPE} = \frac{100\%}{N} \sum_{i=1}^{N} \left| \frac{\hat{B}_i - B(x_i)}{B(x_i)} \right|, \tag{9}$$

where $\hat{B}_i$ is the flexural rigidity recovered at station i, taken either as the uncorrected B_0 or the corrected $B_0 W(m)$. The mean signed percentage error was computed in the same way without the absolute value, to expose any residual systematic bias. The benefit of the correction was assessed by comparing these metrics before and after its application; because this comparison is deterministic for a prescribed profile, no inferential statistical test is involved. To assess robustness to measurement noise, apparent rigidities were generated as in Section 2.4, perturbed by additive Gaussian noise of constant fractional amplitude $\sigma_B(x) = (\sigma_B/B)\,B(x)$, and processed either directly or after a one-dimensional Gaussian filter of physical scale $\sigma_s = 0.75$ cm applied across stations (boundary mode *nearest*, to avoid edge reflections). Errors were averaged over 10^3 Monte Carlo realizations per condition.

3 Results

3.1 Recovering flexural rigidity through a transition zone

We first illustrate the correction on a model device with a compliant region that stiffens linearly to a stiff body across a localized transition zone (Fig. 2). The standard three-point formula, Eq. (1), returns an apparent flexural rigidity that underestimates the true value throughout the transition: by up to $\sim$1.8% here, with the largest error toward the compliant side where the fractional gradient is steepest (Fig. 2b). Estimating the local gradient by windowed regression, Eq. (8), and applying the correction, Eq. (5), recovers the true flexural rigidity to near zero error across the interior of the transition. A residual of $\sim$0.8% remains at the two corners of the ramp, where the flexural rigidity does not vary linearly across the support span and the assumption underlying Eq. (4) is locally violated. This is a limitation we examine for smooth transitions below.

3.2 Error magnitude and the role of measurement spacing

Across a representative gradient spanning the full flexural rigidity range of a device (Fig. 3), the uncorrected reading is accurate over most of the length and departs from the true flexural rigidity only near the most compliant end. The error remains below 1% except at the most compliant station, where the fractional gradient is largest ($m \approx 0.95$, at the edge of the small-gradient regime) and the underestimate reaches $\sim$11% (Fig. 3b). This follows directly from the correction factor: because $W(m)$ is an even function of m with $W(m) \geq 1$ (Eq. (4)), the apparent flexural rigidity *always* underestimates the true midspan flexural rigidity, by an amount that grows as $m^2/10$ with the magnitude of the local gradient and is independent of its sign. The accuracy of the correction is set by how well the local gradient can be estimated, which in turn depends on the measurement spacing. At fine spacing the estimated $m(x)$ tracks the true profile closely, whereas at coarse spacing ($s/L = 3$) it fails to resolve the gradient (Fig. 3d). The mean error over the device accordingly increases with spacing and is reduced by successive iterations of the correction (Fig. 3c); for the spacings used in practical profiling ($s/L \lesssim 0.5$), a few iterations bring the residual to a fraction of a percent.

3.3 Smooth transitions and the curvature limit

To assess the correction's behavior on the smooth flexural rigidity transitions characteristic of real graded catheters, we generated a logistic test profile,

$$B(x) = B_{\min} + \frac{B_{\max} - B_{\min}}{1 + \exp[-\kappa(x - x_t)]}, \tag{10}$$

with $B_{\min} = 4$ N·cm^2, $B_{\max} = 1000$ N·cm^2, $\kappa = 0.5$ cm^{-1}, and $x_t = 10$ cm on a 20 cm beam (Fig. 4a). Apparent rigidities were generated by solving the three-point bend deflection (Eq. (3)) numerically at each

station, identically to the procedure of Section 3.2. With span $L = 3$ cm, the standard uncorrected test recovered the true midpoint flexural rigidity to a mean error of 1.12% and a peak of 2.23%, essentially independent of the station spacing s (Fig. 4c, gray references). For a transition of this character, the three-point reading is already accurate before any correction is applied. The performance of the linear correction, in contrast, depends strongly on spacing (Fig. 4c). At very fine spacing ($s/L = 0.10$) the corrected mean error decreases marginally to 1.06%, but the peak rises to 3.48%. At a practically reasonable spacing of $s/L = 0.25$ the mean grows to 1.39% and the peak to 6.50% (Fig. 4b), with the overcorrection concentrated at the compliant edge of the profile, where B is small and m is large. At coarser spacing the corrected error rises sharply, exceeding 30% in the mean and 75% at the peak by $s/L = 2$. The corrected peak error exceeds the uncorrected peak at every spacing tested. To distinguish error introduced by gradient estimation from a more fundamental limitation, we replaced the windowed-regression slope with the exact secant gradient $m = [B(x+L/2) - B(x-L/2)]/[2B(x)]$ computed analytically from the known profile, and reduced the spacing to $s/L = 0.05$ (Fig. 4d). Even in this idealized limit the corrected mean and peak errors (1.23% and 3.71%) sit above the uncorrected baseline (1.12% and 2.23%), with the residual concentrated at the curvature shoulders of the logistic where $|B''|$ is largest. The closed-form relation $B_0 = B_m/W(m)$ holds exactly only for B linear across the span; for a curved profile no single m satisfies it, and the residual is bounded below by a curvature contribution of order $(L^2/B)\,|B''|$ that the linear theory of Section 2.3 does not capture. Improving the gradient estimate alone cannot recover this term. The practical consequence is a clear scope of application. The closed-form correction is exact for linear gradients and beneficial in regions of a profile where $B(x)$ is approximately linear across the support span, such as the interior of a fabricated linear ramp (Fig. 3) or the steep, near-linear tip region of a graded catheter. For smoothly transitioning regions, the standard three-point reading is already accurate within $\sim 2\%$, and the linear correction should not be applied: it requires impractically fine sampling even to break even on the mean, increases the peak error at every spacing tested, and is bounded by a curvature floor that no improvement in gradient estimation can cross. An extension of the closed-form correction to second order in B'' would in principle address this floor, but robust estimation of B'' from three-point bend data is impractical, and we do not pursue it here.

3.4 Robustness to measurement noise

A correction that is exact in the noiseless limit is only useful insofar as it tolerates the noise of a real instrument. To characterize this tolerance, we generated apparent rigidities for the linear gradient of Section 3.2 ($B = 4 + 49.8x$ N·cm^2 on a 20 cm beam) using the full forward model of Eq. (3), and perturbed each measurement by additive Gaussian noise of constant fractional amplitude $\sigma_B(x) = (\sigma_B/B)\,B(x)$. This "percent-of-reading" convention matches how load-cell precision is typically quoted and gives a spatially uniform signal-to-noise ratio, isolating the role of noise from the geometric variation in deflection across the gradient. Errors were averaged over 10^3 Monte Carlo realizations per condition. Two estimators were compared: the iterative correction of Section 2.4 applied directly to the noisy measurements ("corrected, raw"), and the same correction applied after a one-dimensional Gaussian pre-filter of physical scale $\sigma_s = 0.75$ cm across stations ("corrected, smoothed"), using nearest-neighbor boundary handling to avoid reflection artifacts at the beam ends. In the noiseless limit the corrected mean error sits at $\sim 4 \times 10^{-3}\%$ across all spacings tested (Fig. 5b, dotted line), confirming the closed-form correction is exact for genuinely linear gradients. With 2% noise, the uncorrected mean error grows from 2.1% at $s/L = 0.1$ to 4.2% at $s/L = 1.5$ as coarser sampling concentrates the average on the compliant-tip region where the local gradient m is largest. The corrected raw estimator removes this spacing dependence almost entirely, holding $\sim 1.5\%$ MAPE across two decades of spacing. Pre-smoothing adds further benefit at fine spacing, reducing MAPE to 0.9% at $s/L = 0.1$, but its advantage vanishes at coarse spacing where the filter has too few neighboring stations to average effectively. The trade-off between bias reduction and noise sensitivity is set by the noise amplitude. At fixed practical spacing $s/L = 0.25$ (Fig. 5c), three regimes are evident. Below $\sigma_B/B \approx 2\%$, the correction alone is

the best estimator: at $\sigma_B/B = 0.5\%$ it yields MAPE $= 0.4\%$, roughly three times better than smoothing-then-correcting (1.0%), because at this noise level the bias the correction removes dominates the residual variance, and any pre-smoothing attenuates the very gradient signal the correction needs. Between 2% and 5% noise the two estimators perform comparably. Above $\sigma_B/B \approx 5\%$ the noise variance dominates, the smoothing attenuates it faster than it blurs the gradient, and smoothing-then-correcting becomes the best estimator; at $\sigma_B/B = 20\%$ it yields MAPE $= 9.0\%$ versus 15.6% for the corrected raw estimator and 15.9% uncorrected. In practice, the noise floor of the rig of Section 2.1 sits below 1% on repeated measurements of a uniform beam, placing the present application firmly in the bias-dominated regime where the correction alone is appropriate. For higher-noise applications such as miniaturized devices and *in situ* tissue measurements, the smoothing length σ_s becomes a tunable parameter; we found that setting σ_s to roughly one-quarter of the test span L gave a favorable trade-off across the noise levels examined, but a brief sensitivity analysis is advisable when the rig and specimen differ substantially from those considered here.

3.5 Application to a commercial graded long sheath

As a demonstration of the correction on a clinically deployed graded device, we analysed bench three-point bend data on the 088 Neuron MAX (Penumbra Inc.) long sheath, with 2.77 mm ($\sim$ 8 French) outer diameter, a device used as a distal-access conduit for stroke thrombectomy and aneurysm interventions. The 088 Neuron MAX long sheath has an intentionally graded shaft that transitions from a compliant distal tip to a torque-stable proximal shaft to balance trackability against support. The device was tested at a sequence of stations along its working length, with three independent test repeats per station on the rig described in Section 2.1. We report the per-station mean B_0 and the standard deviation across repeats as a direct measure of within-station uncertainty. The device was tested at 18 stations spanning $x = 2$ cm (distal) to $x = 43$ cm (proximal), with 1 cm spacing through the transition region and 5 cm spacing along the uniform shaft. The bend span was $L = 3$ cm, identical to the synthetic studies of Sections 3.2 and 3.3. Per-station mean rigidities $B_0(x)$ were pre-smoothed with a Gaussian filter of physical scale $\sigma_s = 0.75$ cm, converted to an index sigma using the median station spacing so the effective smoothing length remained constant across the device's piecewise-uniform sampling. The iterative correction of Section 2.4 was then applied, with the local gradient estimated by linear regression over a 4 cm physical window centred on each station (rather than a fixed number of neighbouring indices, which would give different effective window lengths in the dense and sparse sampling regions). Uncertainty was propagated by Monte Carlo: 2×10^3 realisations were drawn from a normal distribution with mean $B_0(x)$ and standard deviation equal to the per-station standard error of the mean ($\mathrm{Err}/\sqrt{3}$), each was processed through the full smoothing plus correction pipeline, and the empirical standard deviation across realisations defined the corrected uncertainty $\sigma_{B_m}(x)$. The Neuron MAX profile (Fig. 6a) shows the expected soft-to-stiff transition: B_0 rises from 1.8 N·cm^2 at the distal tip to a plateau of ≈ 16 N·cm^2 along the shaft, with the transition centred near $x = 10$ cm and substantially complete by $x = 18$ cm. Beyond the transition, the four shaft stations ($x = 18$ to 43 cm) sit within ± 1.2 N·cm^2 of one another, confirming that the proximal shaft is mechanically uniform at the resolution of the bend test. Across-repeat measurement uncertainty was modest: the median relative standard deviation was 1.72%, with $\mathrm{Err}/B_0 \leq 2.8\%$ at all but one station. The exception is the distal tip station at $x = 2$ cm, where $\mathrm{Err}/B_0 = 10.3\%$, consistent with the difficulty of repeatable placement on a very compliant element at the end of the device. The local gradient $m(x)$ extracted from the smoothed profile (Fig. 6b, magenta) peaks at $m = 0.34$ at $x = 7$ cm, in the middle of the transition. This is comparable to the peak gradients encountered in the synthetic logistic profile of Section 3.3 and well within the regime where the closed-form correction $W(m)$ is expected to be accurate for the locally near-linear shape of the transition shoulder. The applied correction (Fig. 6b, blue, right axis) reaches $W(m) - 1 = 1.2\%$ at the same station and is below 0.1% along the uniform shaft, where $m \approx 0$ to numerical precision. Averaged over the device the absolute correction is 0.5%, which is small in relative terms but systematically biased in one direction: every station in the transition region has its flexural rigidity

revised upward, as expected from the sign-independent bias property of the linear correction (Section 2.3). For this device the $W(m)$ correction is smaller than the median measurement noise (1.2% peak versus 1.7% median noise), placing the application at the boundary between the bias-dominated and noise-dominated regimes identified in Section 3.4. The bias removal is real and resolvable: the propagated standard deviation of B_m in the transition region is ≈ 0.05 N·cm^2, much smaller than the 1.2% shift imposed by $W(m)$. The practical significance, however, is modest, since a clinician selecting between devices on the basis of these measurements would not change their decision based on a 1% revision of the transition flexural rigidity. The correction's value here is principally that it removes a known systematic bias from a measurement that is otherwise reported and compared across devices and across laboratories, not that it changes the device's characterisation in any clinically meaningful way. The picture would differ for a device with a steeper short-length transition, where peak m approaches the range (0.5–0.7) at which $W(m)$ corrections of 5–20% become material; the 088 Neuron MAX, with its deliberately gradual transition over ~ 10 cm, was engineered to avoid exactly that regime.

4 Discussion

This closed-form correction for the systematic error introduced by linear flexural rigidity gradients in three-point bend testing of functionally graded beams yields a correction factor $W(m)$ of Eq. (4), exact in the absence of measurement noise. Its series expansion (Eq. (6)) has a leading-order term $W(m) \approx 1 + m^2/10$ that makes the bias magnitude predictable from a single dimensionless gradient parameter. The correction is sign-independent: because $W(m)$ is an even function with $W(m) \geq 1$, the apparent flexural rigidity always underestimates the true midspan flexural rigidity, regardless of whether the gradient is positive or negative. The $m^2/10$ scaling explains why standard three-point testing performs as well as it does on most clinically deployed graded devices: even at the steepest local gradient encountered on the 088 Neuron MAX (Section 3.5), $m = 0.34$, the predicted bias is 1.2%, comparable to the across-repeat noise of a careful bench measurement. The closed-form result is exact for gradients that are linear across the test span L, and the regime maps of Sections 3.3 and 3.4 delimit where this exactness translates into practical value. For genuinely linear gradients (Section 3.2) the correction recovers the true flexural rigidity profile to numerical precision in the noiseless limit and to within a fraction of a percent in the presence of measurement noise below 2%. For the smooth transitions characteristic of clinically deployed graded catheters, this floor is modest in absolute terms ($\sim 1\%$ mean error) but it sits above the uncorrected baseline. The correction should therefore not be applied in this regime; the standard three-point test is already accurate to within the rig's noise, and applying the linear correction degrades rather than improves the estimate. The 088 Neuron MAX analysis is representative of contemporary graded long sheaths and shows the correction operating at modest magnitude. The largest $W(m)$ correction was 1.2% at the steepest point of the transition; the device's noise floor of $\sim 1.7\%$ across repeats places this application at the boundary between the bias-dominated and noise-dominated regimes. The correction's value here is not that it changes the device's clinical characterisation, as a 1% revision of transition flexural rigidity would not alter the choice between this sheath and a competing one. Instead, the value is that it removes a known systematic component of the bench measurement. This matters chiefly for cross-laboratory comparison, where rigs with different test spans, different sampling densities, and different calibration histories report flexural rigidities that carry the gradient bias to different degrees. A device with a more abrupt transition, or a test protocol with a longer span relative to the transition length, would show proportionally larger corrections, and the framework here makes the size predictable in advance from a single dimensionless ratio. The forward problem of bending in functionally graded beams is mature in the FGM and AFG literatures [18–22], with closed-form, semi-analytic, and finite element solutions for an extensive variety of grading laws and boundary conditions. The closest prior art on the inverse problem is the numerical iterative identification of [31], which recovers a position-dependent flexural rigidity from a series of bend tests by repeated forward modelling. The closed-form correction presented here is the

explicit analytical solution to a restricted case of that inverse problem (the linear gradient), and its principal advantage over numerical inversion is interpretive rather than computational. The $m^2/10$ leading order makes the bias magnitude calculable from inspection, and the closed form admits the asymptotic analysis that delivers the regime map of Section 3.4. For non-linear gradients the iterative scheme of Lucchinetti and Knecht remains the appropriate tool, with the caveat that its outputs inherit a sensitivity to B'' over the test span that any local linearisation must share. Several limitations and extensions remain. The analysis assumed pure Euler-Bernoulli flexural response, neglecting shear deformation; for graded devices with small cross-section relative to the test span this is justified along most of the working length, but warrants more careful examination at the compliant distal tip where the slenderness ratio can become marginal. We assumed a prismatic cross-section, which is appropriate for the long sheaths considered here but not for tapered tip catheters where the cross-section itself varies along the device; the correction would in principle generalise, with W becoming a functional of the local geometric profile rather than a function of a single gradient. The curvature-limited floor identified in Section 3.3 is in principle removable by a second-order extension carrying a B'' term, but the practical obstacle to such an extension is the difficulty of estimating B'' reliably from noisy bend data: the regression that produced the local gradient m here is already near the limit of what the noise budget supports, and a second derivative would require either substantially denser sampling or a tightly constrained parametric form. Beyond endovascular devices, the same framework applies wherever three-point bend testing is performed on materials with intentional or natural property gradients, including the plant stalks and bamboo internodes [26–28] that motivated parts of the present work, additively manufactured parts with graded infill density, and graded biomaterials more generally. The $m^2/10$ rule provides a quick, calculator-free estimate of when such measurements require correction and when they can be reported as measured.

5 Conclusions

We have derived a closed-form correction $W(m)$ that recovers the true midspan flexural rigidity of a linearly graded beam from a standard three-point bend measurement, exactly in the absence of measurement noise. The expansion $W(m) = 1 + m^2/10 + m^4/35 + m^6/84 + \cdots$ reduces in its leading term to a single dimensionless rule: the relative bias of an apparent flexural rigidity measurement is approximately $m^2/10$, where m is the local gradient parameter at the test station. The correction is sign-independent: $W(m) \geq 1$ for all $|m| < 1$. Thus, the apparent flexural rigidity always underestimates the true value, regardless of whether $B(x)$ is locally increasing or decreasing. The closed form is exact for gradients that are linear across the test span; it should not be applied otherwise. For smooth profiles whose curvature varies across the span, including the typical transitions of clinically deployed graded devices, the standard three-point bend test is already accurate to within $\sim$ 1–2%, and the linear correction is bounded below by a curvature-limited residual that no improvement in gradient estimation can remove. A simple two-step decision rule follows. If $B(x)$ is approximately linear across L, apply the correction directly when the measurement noise satisfies $\sigma_B/B \lesssim 2\%$, and pre-smooth before correction when it does not. Otherwise, report the apparent flexural rigidity as measured. Applied to bench data on the 088 Neuron MAX long sheath, the correction reached 1.2% at the steepest point of the device's distal transition, comparable to the across-repeat measurement noise of the rig. The framework presented here is portable to any three-point bend test on a material with a known or suspected flexural rigidity gradient, from engineered functionally graded composites and additively manufactured parts to graded biological beams. In every such application, the $m^2/10$ rule provides a calculator-free first estimate of whether the apparent flexural rigidity requires correction before it can be reported with confidence.

Ethics. This study involved bench mechanical testing of commercial medical devices only; no human participants, human data, or animals were used, and no ethical approval was required.

Data accessibility. The bench three-point bend data and the analysis/correction code supporting this article

will be deposited in Zenodo upon publication.

Authors' contributions. C.B.S., J.J.B.-G., and M.Y.Q. performed the experiments and analysis and developed the apparatus and software; M.A.Z. and J.W.O. provided clinical guidance and devices; C.B.S., J.J.B.-G., Y.E.G, Y.H., and G.M.G. derived the correction and validated it. All authors read and approved the manuscript.

Competing interests. J.W.O. serves as a consultant for Terumo, Inc., Microvention, Inc., Stryker, Inc., Medtronic, Inc., and Penumbra, Inc., and receives research support from Microvention, Inc. G.M.G. and M.A.Z. own interest in Caeli Vascular, Inc. G.M.G, J.W.O., and M.A.Z. own interest in Vascorra, LLC. M.A.Z. owns interest in AirSeal Cardiovascular, LLC. C.B.S., J.J.B.-G., Y.E.G, M.Y.Q., and Y.H. declare no competing interests.

Funding. This work was funded in part by the NIH through grants R41HL150963, R42HL150963, and T32HL170959; the Center for Innovation in Neuroscience and Technology at Washington University; and the Jeffrey Fort Cerebrovascular Innovation Fund to the Department of Neurosurgery at Washington University in St. Louis School of Medicine.

A Closed-form solution for the linearly graded beam

Let $w(x)$ denote the deflection in the direction of the applied load. Under Euler-Bernoulli theory the deflection satisfies Eq. (3),

$$B(x)\,\frac{\mathrm{d}^2 w}{\mathrm{d}x^2} = -\frac{F}{2}\left(\frac{L}{2} - |x|\right), \tag{11}$$

with $B(x) = B_m(1+2mx/L)$ and supports at $x = \pm L/2$. We non-dimensionalize using the normalized flexural rigidity coordinate $Y = 1+2mx/L$ (so that $B = B_m Y$, with $Y = 1$ at midspan and $Y = 1 \pm m$ at the supports) and the normalized deflection $W = w/w_0$, where $w_0 = FL^3/(48B_m)$. Noting that $\mathrm{d}^2/\mathrm{d}x^2 = (2m/L)^2\,\mathrm{d}^2/\mathrm{d}Y^2$, and that $\frac{L}{2} - |x|$ equals $\frac{L}{2m}[(1+m)-Y]$ on the right half and $\frac{L}{2m}[Y-(1-m)]$ on the left, Eq. (11) reduces to

$$\frac{\mathrm{d}^2 W}{\mathrm{d}Y^2} = \begin{cases} \dfrac{3}{m^3}\left(1 - \dfrac{1+m}{Y}\right), & 1 \le Y \le 1+m, \\[2ex] \dfrac{3}{m^3}\left(\dfrac{1-m}{Y} - 1\right), & 1-m \le Y \le 1. \end{cases} \tag{12}$$

Integrating twice on each interval, and writing $g(Y) \equiv Y\ln Y - Y$,

$$W_{\mathrm{R}}(Y) = \frac{3}{m^3}\left[\frac{Y^2}{2} - (1+m)\,g(Y)\right] + a_1 Y + a_2, \tag{13}$$

$$W_{\mathrm{L}}(Y) = \frac{3}{m^3}\left[(1-m)\,g(Y) - \frac{Y^2}{2}\right] + b_1 Y + b_2. \tag{14}$$

The four constants are fixed by zero deflection at the supports, $W_{\mathrm{R}}(1+m) = W_{\mathrm{L}}(1-m) = 0$, together with continuity of deflection and slope at the loading point, $W_{\mathrm{R}}(1) = W_{\mathrm{L}}(1)$ and $W'_{\mathrm{R}}(1) = W'_{\mathrm{L}}(1)$. The two continuity conditions give

$$b_1 - a_1 = \frac{6}{m^3}, \qquad a_2 - b_2 = -\frac{3}{m^3}, \tag{15}$$

and the central deflection is $W(0) = W_{\mathrm{R}}(1) = \frac{3}{m^3}\left(\frac{3}{2} + m\right) + a_1 + a_2$. Solving the four conditions for the constants and evaluating at $Y = 1$ yields

$$W(m) \equiv \frac{w(0)}{w_0} = \frac{3}{2m^3}\Big[(1+m)^2\ln(1+m) - (1-m)^2\ln(1-m) - 2m\Big], \tag{16}$$

which is Eq. (4). Expanding the logarithms about $m = 0$ recovers the series of Eq. (6),

$$W(m) = 1 + \frac{m^2}{10} + \frac{m^4}{35} + \frac{m^6}{84} + \frac{m^8}{165} + \cdots = \sum_{k=0}^{\infty} \frac{m^{2k}}{\binom{2k+3}{3}}. \tag{17}$$

References

[1] Olvert A Berkhemer, Puck SS Fransen, Debbie Beumer, et al. A randomized trial of intraarterial treatment for acute ischemic stroke. *New England Journal of Medicine*, 372:11–20, 2015.

[2] Mayank Goyal, Andrew M Demchuk, Bijoy K Menon, et al. Randomized assessment of rapid endovascular treatment of ischemic stroke. *New England Journal of Medicine*, 372:1019–1030, 2015.

[3] Tudor G Jovin, Angel Chamorro, Erik Cobo, et al. Thrombectomy within 8 hours after symptom onset in ischemic stroke. *New England Journal of Medicine*, 372:2296–2306, 2015.

[4] Michael Y Qiu, Charles B Suskin, Mohamed A Zayed, Guy M Genin, and Joshua W Osbun. Energy barriers govern catheter herniation during endovascular procedures: a 2.5 d vascular flow model analysis. *Journal of the Royal Society Interface*, 21(219), 2024.

[5] Zeliha Oksan Kaymaz, O Nikoubashman, MA Brockmann, M Wiesmann, and C Brockmann. Influence of carotid tortuosity on internal carotid artery access time in the treatment of acute ischemic stroke. *Interventional Neuroradiology*, 23(6):583–588, 2017.

[6] T Brandt, R Schmidt, and K Johnson. Cardiovascular catheters: material composition, structural design, and catheter tip options. *Cardiovascular Engineering and Technology*, 12:234–248, 2021.

[7] Chase M Hartquist, Jin Vivian Lee, Michael Y Qiu, Charles Suskin, Vinay Chandrasekaran, Halle R Lowe, Mohamed A Zayed, Joshua W Osbun, and Guy M Genin. Stability of navigation in catheter-based endovascular procedures. *bioRxiv*, pages 2023–06, 2023.

[8] Mark C Horattas, John Trupiano, Steve Hopkins, Debbie Pasini, Carl Martino, and Aparna Murty. Changing concepts in long-term central venous access: catheter selection and cost savings. *American journal of infection control*, 29(1):32–40, 2001.

[9] Sidhi Laksono, R Mohammad Reza Juniery Pasciolly, Haris Munirwan, Ahmad Pandu Pratama, and Ananta Siddhi Prawara. Choosing the appropriate catheter and wire in peripheral intervention. *AsiaIntervention*, 8(2):162, 2022.

[10] Chase M Hartquist, Vinay Chandrasekaran, Halle Lowe, Eric C Leuthardt, Joshua W Osbun, Guy M Genin, and Mohamed A Zayed. Quantification of the flexural rigidity of peripheral arterial endovascular catheters and sheaths. *Journal of the mechanical behavior of biomedical materials*, 119:104459, 2021.

[11] M Y Qiu, C B Suskin, J J Becerra-Garcia, S H Roberts, D G Rucker, M A Zayed, J W Osbun, and G M Genin. Quantification of the flexural rigidity of endovascular surgical devices using three-point bending tests. *Research Square*, 2023. Preprint.

[12] ASTM. Standard test method for three-point bending of balloon expandable vascular stents and stent systems, 2021. ASTM F2606-08.

[13] A Carl Maki and Edward W Kuenzi. *Deflection and stresses of tapered wood beams*, volume 34. Madison: US Department of Agriculture, Forest Service, Forest Products Laboratory, 1965.

[14] William J McCutcheon. Deflections and stresses in circular tapered beams and poles. *Civil Engineering for Practicing and Design Engineers*, 2:207–233, 1983.

[15] JR Banerjee and FW Williams. Exact bernoulli-euler static stiffness matrix for a range of tapered beam-columns. *International Journal for Numerical Methods in Engineering*, 23(9):1615–1628, 1986.

[16] Nathanael Martin-Nelson, Brandon Sutherland, Michael Yancey, Chung Shan Liao, Christopher J Stubbs, and Douglas D Cook. Axial variation in flexural stiffness of plant stem segments: measurement methods and the influence of measurement uncertainty. *Plant Methods*, 17(1):101, 2021.

[17] Juergen Schoeftner. Stress distribution and deflection of symmetric tapered beams. *Acta Mechanica*, 236(3):1883–1898, 2025.

[18] B. V. Sankar. An elasticity solution for functionally graded beams. *Composites Science and Technology*, 61(5):689–696, 2001.

[19] Y. Huang and X.-F. Li. A new approach for free vibration of axially functionally graded beams with non-uniform cross-section. *Journal of Sound and Vibration*, 329(11):2291–2303, 2010.

[20] M. Aydogdu. Semi-inverse method for vibration and buckling of axially functionally graded beams. *Journal of Reinforced Plastics and Composites*, 27(7):683–691, 2008.

[21] I. Elishakoff and S. Candan. Apparently first closed-form solution for vibrating inhomogeneous beams. *International Journal of Solids and Structures*, 38(19):3411–3441, 2001.

[22] I. Elishakoff and Z. Guédé. Analytical polynomial solutions for vibrating axially graded beams. *Mechanics of Advanced Materials and Structures*, 11(6):517–533, 2004.

[23] Bernard Budiansky and George F Carrier. The pointless wedge. *SIAM Journal on Applied Mathematics*, 25(3):378–387, 1973.

[24] P Ruta and J Szybiński. Nonlinear analysis of nonprismatic timoshenko beam for different geometric nonlinearity models. *International Journal of Mechanical Sciences*, 101:349–362, 2015.

[25] Krzysztof Magnucki, Jerzy Lewinski, Mariusz Far, and Piotr Michalak. Three-point bending of an expanded-tapered sandwich beam – analytical and numerical fem study. *Mechanics Research Communications*, 103:103471, 2020.

[26] Ulrike GK Wegst and Michael F Ashby. The structural efficiency of orthotropic stalks, stems and tubes. *Journal of Materials Science*, 42(21):9005–9014, 2007.

[27] Ulrike GK Wegst. Bending efficiency through property gradients in bamboo, palm, and wood-based composites. *Journal of the mechanical behavior of biomedical materials*, 4(5):744–755, 2011.

[28] Kaiyang Yin, Max D Mylo, Thomas Speck, and Ulrike GK Wegst. Bamboo-inspired tubular scaffolds with functional gradients. *Journal of the Mechanical Behavior of Biomedical Materials*, 110:103826, 2020.

[29] Wenchao Wu, Yongguang Hu, and Zehui Jiang. Investigation on the bending behavior of tea stalks based on non-prismatic beam with virtual internodes. *Agriculture*, 12(3):370, 2022.

[30] Mahsa Zojaji, Baixuan Yang, Caitlyn J Collins, Thomas D Crenshaw, and Heidi-Lynn Ploeg. Accurate measurement of a bone surrogate flexural rigidity in three-and four-point bending. *Journal of the Mechanical Behavior of Biomedical Materials*, page 106986, 2025.

[31] E. Lucchinetti and E. Stüssi. Measuring the flexural rigidity in non-uniform beams using an inverse problem approach. *Inverse Problems*, 18(3):837–857, 2002.

[32] Stephen Timoshenko. *Strength of Materials Part I: Elementary Theory and Problems*. New York: Van Nostrand, 1940.

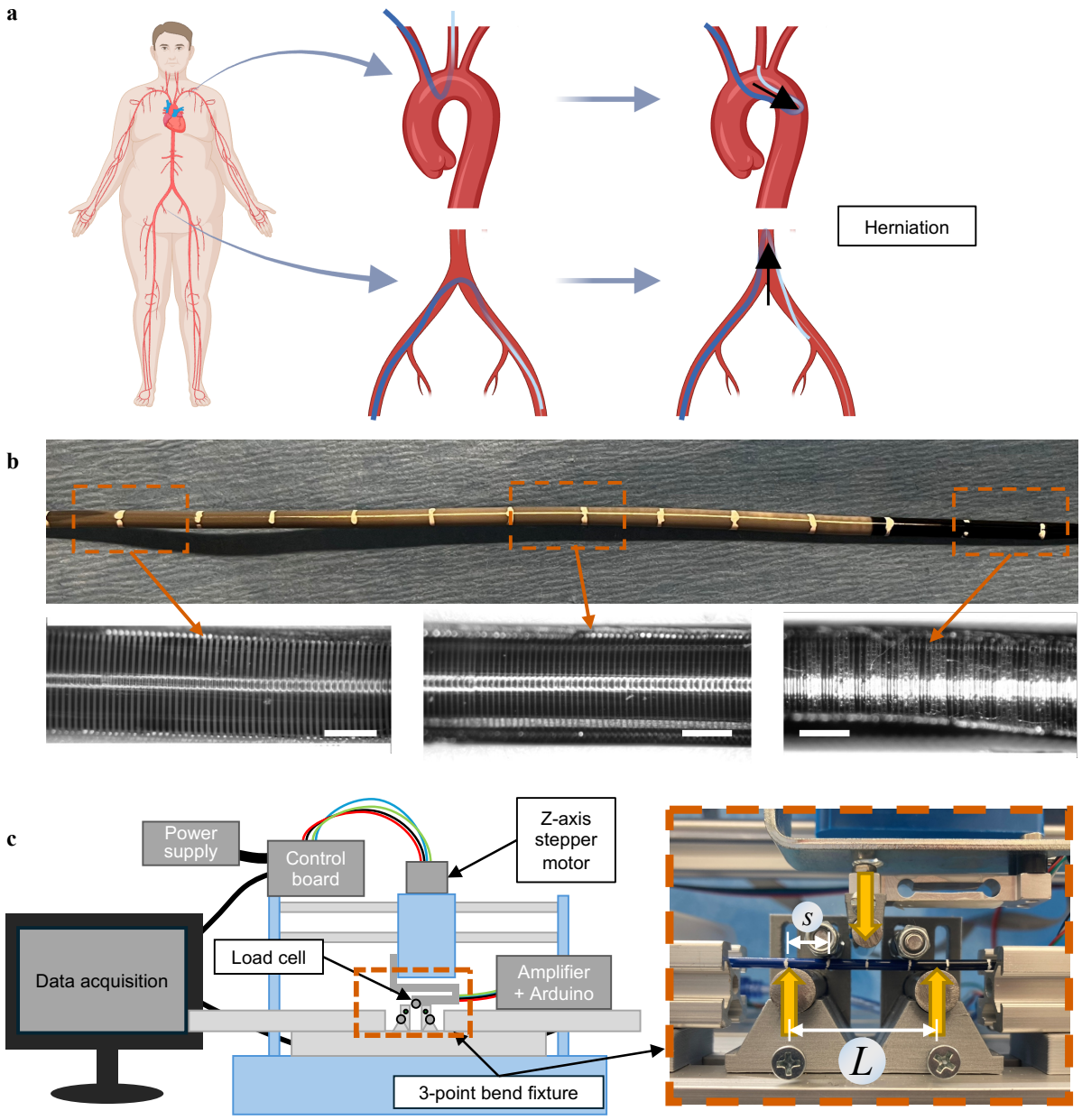

Figure 1. Endovascular devices have engineered flexural rigidity gradients that govern navigation and must be characterized along their length. **(a)** Insufficient flexural rigidity causes a device to herniate out of its intended path at a sharp bend, losing the support needed to reach the distal target. In trans-radial access to the cerebral vasculature, a device advanced through the aortic arch can prolapse downward into the descending thoracic aorta (top); in contralateral access from a femoral approach, a device crossing the aortic bifurcation can herniate upward into the abdominal aorta (bottom). Panel (a) was created using biorender.com. **(b)** A commercial neurovascular long sheath (088 Neuron MAX, Penumbra, Inc.) is built with flexural rigidity that varies along its length. Magnified views show the stiff proximal body, the graded transition zone, and the compliant distal tip (scale bar, 1 mm). **(c)** Flexural rigidity is profiled by three-point bending. A schematic of the apparatus (left) and a photograph of the test region (right) define the support span L and the spacing s between successive measurement stations along the device.

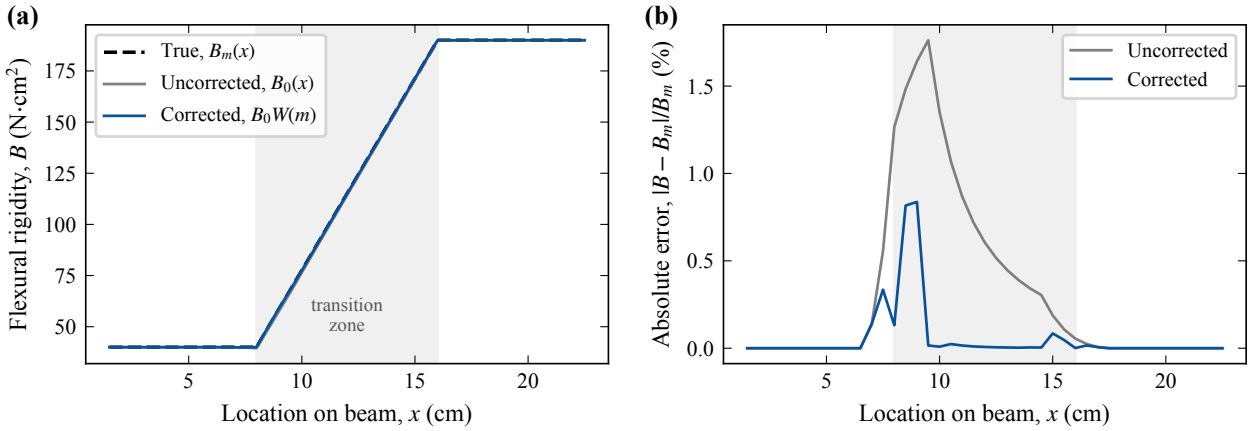

Figure 2. The three-point bend reading carries a systematic error localized to a stiffness transition zone, which the closed-form correction removes. A model device with a compliant region ($B = 40$ N·cm^2) stiffening linearly to a stiff region ($B = 190$ N·cm^2) across a transition zone (shaded, 8–16 cm), profiled with a support span $L = 3$ cm. **(a)** Flexural rigidity profile: the true midspan flexural rigidity $B_m(x)$ (dashed), the uncorrected three-point reading $B_0(x)$, and the corrected estimate $B_0 W(m)$ are nearly indistinguishable on the flexural rigidity axis. **(b)** The same data as absolute percentage error. The uncorrected reading underestimates the true flexural rigidity by up to $\sim$1.8% within the transition, largest toward the compliant side where the fractional gradient is steepest, and the correction reduces this to near zero. The small residual peaks at the two corners arise because the correction assumes a flexural rigidity that varies linearly across the support span, an assumption violated where the gradient changes abruptly.

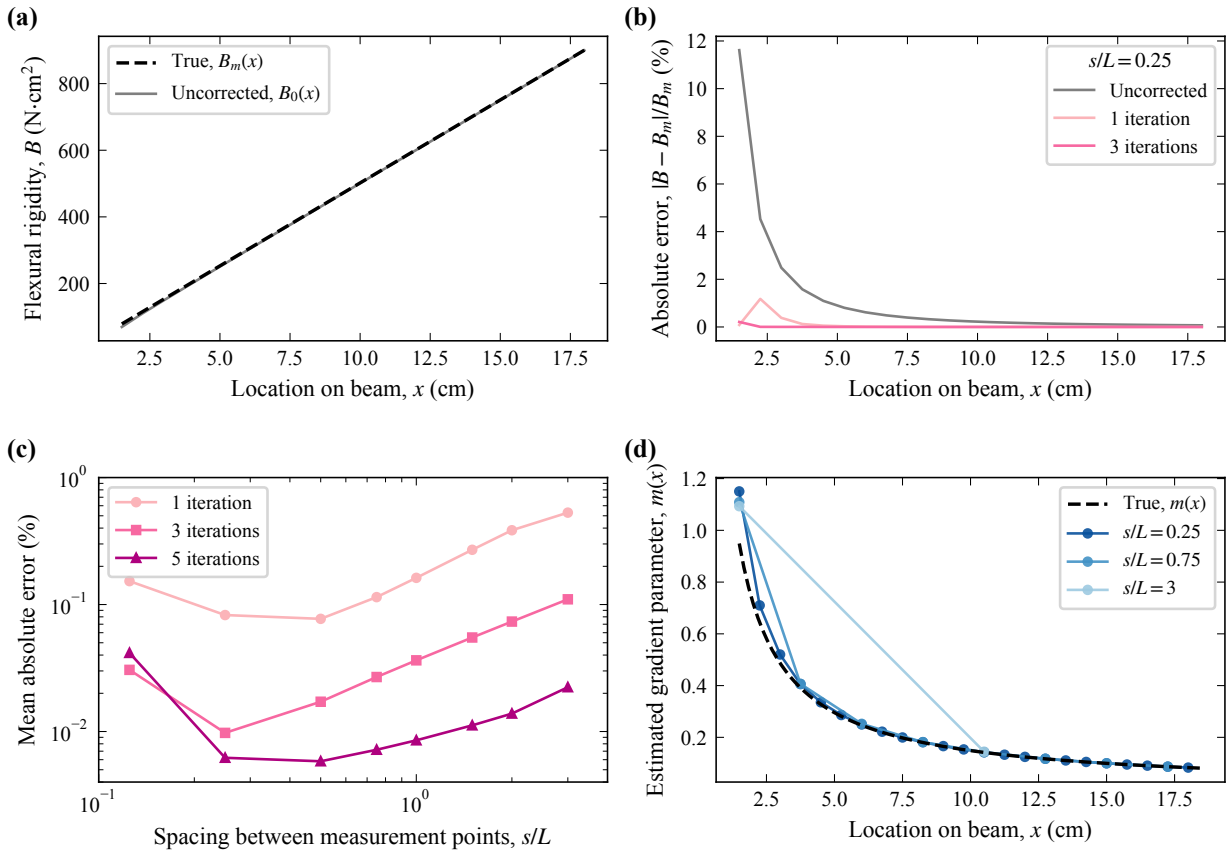

Figure 3. Across a representative flexural rigidity gradient the uncorrected reading is accurate except near the very compliant end, and the accuracy of the correction is governed by the measurement spacing. A beam whose flexural rigidity increases linearly from $B = 4$ to 1000 N·cm^2 over a 20 cm graded region, profiled with a support span $L = 3$ cm. **(a)** The true midspan flexural rigidity $B_m(x)$ (dashed) and the uncorrected reading $B_0(x)$ are visually indistinguishable over most of the device. **(b)** Absolute percentage error along the beam at a spacing $s/L = 0.25$. The uncorrected reading underestimates the true flexural rigidity by $\sim$11% only at the most compliant end, where the fractional gradient is largest ($m \approx 0.95$, near the limit of the small-gradient regime), and falls below 1% within a few centimetres; one and three iterations of the correction reduce the error to near zero. **(c)** Mean absolute error over the device as a function of measurement spacing s/L, for one, three and five correction iterations. Error grows with coarser spacing and is reduced by successive iterations. **(d)** Estimated gradient parameter $m(x)$ for three spacings, compared with the true $m(x)$ (dashed). Coarse spacing ($s/L = 3$) fails to resolve the gradient, which is the source of the spacing dependence in panel (c).

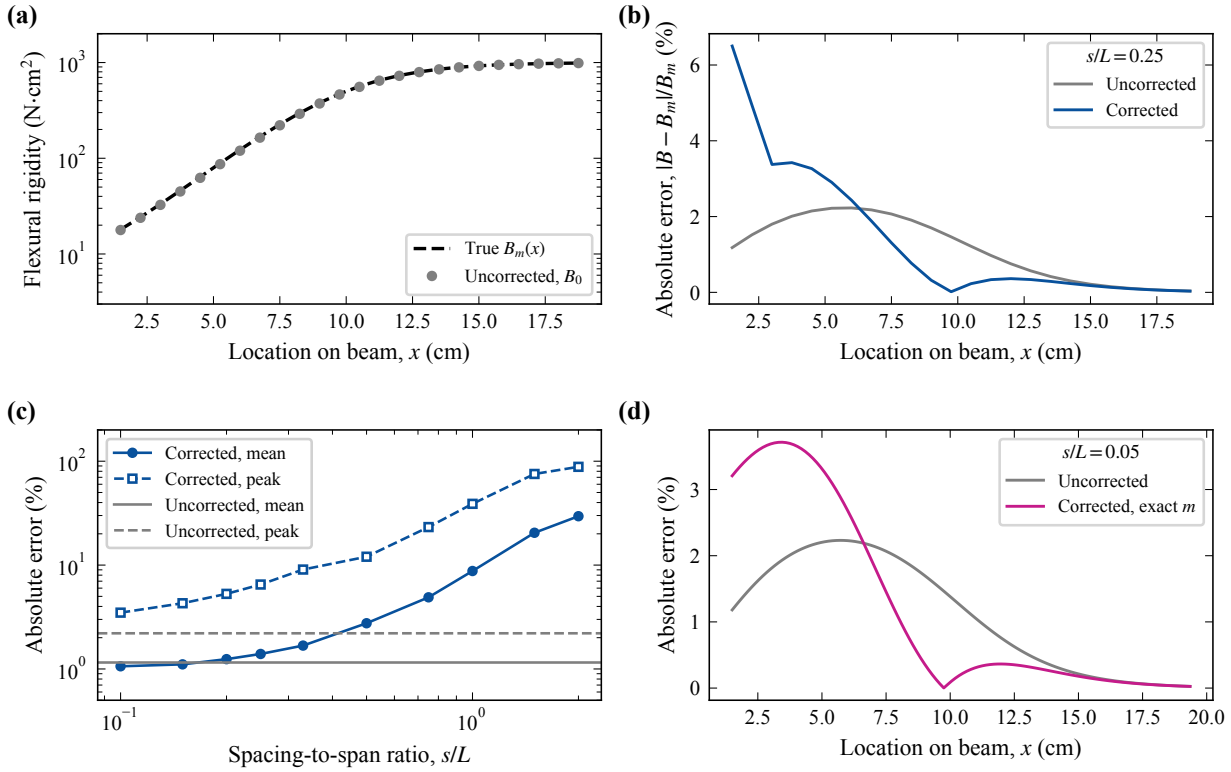

Figure 4. The linear correction on a smooth (logistic) flexural rigidity transition. (a) Test profile: $B(x)$ varies sigmoidally from $B_{\min} = 4$ to $B_{\max} = 1000$ N·cm^2 over a 20 cm beam ($\kappa = 0.5$ cm^{-1}, $x_t = 10$ cm), with uncorrected three-point readings (gray circles) at $s/L = 0.25$ tracking the true profile (dashed). (b) Absolute error at the same spacing: the uncorrected error (gray) remains below 2.23%, while the linear correction (blue) overshoots near the compliant edge where B is small and the local gradient m is large, reaching a peak of 6.50%. (c) Mean (•) and peak (□) corrected error versus spacing-to-span ratio s/L; the spacing-independent uncorrected baselines (gray solid, mean; gray dashed, peak) are shown for reference. The corrected mean meets the uncorrected baseline only as $s/L \to 0$, and the corrected peak exceeds the uncorrected peak at every spacing tested. (d) Curvature-limited floor: at $s/L = 0.05$ with the exact secant gradient $m = [B(x+L/2) - B(x-L/2)]/[2B(x)]$ computed analytically from $B(x)$ (rather than estimated by regression), the corrected error (magenta) still sits above the uncorrected baseline (gray) at the shoulders of the logistic, where $|B''|$ is largest. This residual is the curvature contribution that the linear closed form cannot capture; no improvement in gradient estimation can remove it.

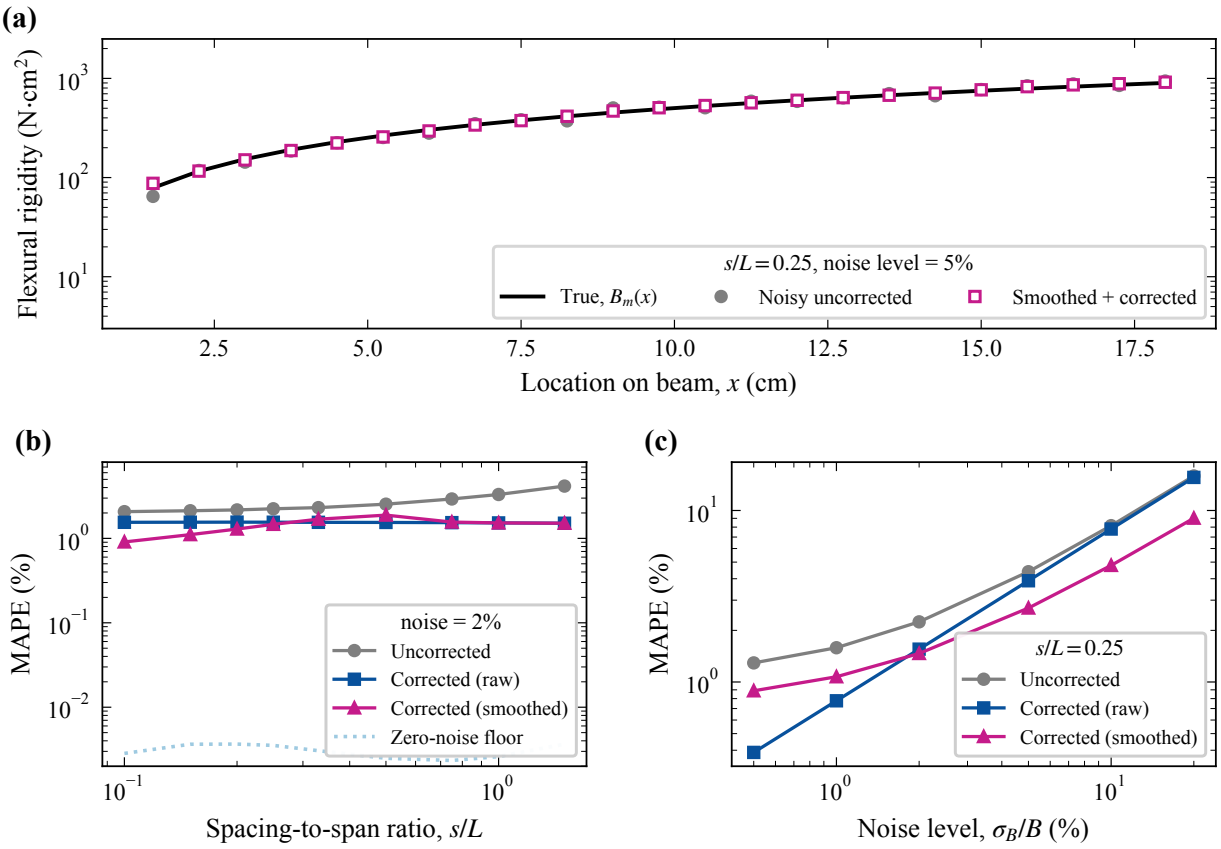

Figure 5. Noise sensitivity on a linear gradient. Test profile $B(x) = 4 + 49.8\,x$ N·cm^2 ($4 \to 1000$ N·cm^2 over 20 cm), $L = 3$ cm. Noise is constant fractional, $\sigma_B(x) = (\sigma_B/B)\,B(x)$; pre-smoothing uses a Gaussian filter with $\sigma_s = 0.75$ cm. Each MAPE point is the mean over 1000 trials. (a) One realization at $s/L = 0.25$ with $\sigma_B/B = 5\%$: smoothed and corrected estimates (open squares) track the true profile (solid line) across more than two decades of flexural rigidity. (b) MAPE versus spacing-to-span ratio at $\sigma_B/B = 2\%$. The corrected raw estimate is flat with spacing; smoothing improves the estimate further at fine spacing and collapses onto the corrected raw curve at coarse spacing, where the filter has no effective neighbors to average. The zero-noise floor confirms that the closed-form correction is exact in the noiseless limit. (c) MAPE versus noise level at $s/L = 0.25$. Below $\sigma_B/B \approx 2\%$ the correction alone is the best estimator; pre-smoothing oversmooths the gradient signal and is counterproductive. Above $\sigma_B/B \approx 5\%$ pre-smoothing reduces noise variance faster than it blurs the gradient, and smoothing-then-correcting becomes the best estimator; at $\sigma_B/B = 20\%$ it nearly halves the MAPE relative to either alternative.

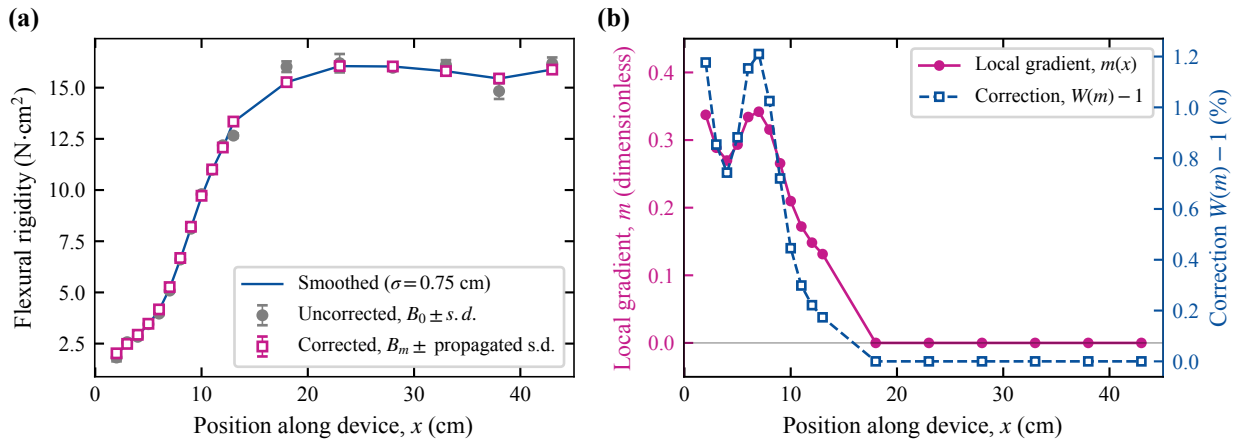

Figure 6. Application of the closed-form correction to bench data on the 088 Neuron MAX long sheath. (a) Apparent (uncorrected, grey) and corrected (magenta) flexural rigidity along the device at 18 stations. Uncorrected error bars are the across-repeat standard deviation; corrected error bars are the standard deviation across 2×10^3 Monte Carlo realisations of the smoothing-plus- correction pipeline, propagating the per-station standard error of the mean. The blue line is the Gaussian-smoothed profile ($\sigma_s = 0.75$ cm in physical units) on which the correction operates. The compliant distal tip transitions to a uniform proximal shaft over $x \approx 6$ to 18 cm. (b) Local gradient $m(x)$ from the smoothed profile (magenta, left axis) and the corresponding correction $W(m) - 1$ (blue, right axis). Both peak at $x = 7$ cm with $m = 0.34$ and $W(m) - 1 = 1.2\%$, and both fall essentially to zero along the uniform shaft. The correction is everywhere positive in the transition region, consistent with the sign-independent bias property of $W(m) \geq 1$.